A two-dimensional computational methodology for high-speed dislocations in high strain-rate deformation

Roos, A; de Hosson, J.T.M.; van der Giessen, E.

Published in:
Computational Materials Science

DOI:
10.1016/S0927-0256(00)00117-8

ELSEVIER

Computational Materials Science 20 (2001) 1–18

COMPUTATIONAL MATERIALS SCIENCE

www.elsevier.com/locate/commatsci

A two-dimensional computational methodology for high-speed dislocations in high strain-rate deformation

A. Roos [a], J.Th.M. De Hosson [a,*], E. Van der Giessen [b]

[a] *Laboratory of Applied Physics, Materials Science Center, Netherlands Institute for Metals Research, University of Groningen, Nijenborgh 4, 9747 AG Groningen, The Netherlands*

[b] *Koiter Institute, Micromechanics of Materials Group, Netherlands Institute for Metals Research, Delft University of Technology, Mekelweg 2, 2628 CD Delft, The Netherlands*

Received 17 April 2000; accepted 16 May 2000

Abstract

In this paper, shear deformation at high strain rates is modeled within the framework of discrete dislocation plasticity. The total stress and deformation state is split into the state due to the dislocations in an infinite medium and the complementary image field, which is enforced by a finite element solution. The stress and displacement fields for high-speed dislocations are used, as well as a velocity-dependent drag coefficient. Sources and obstacles are put into the material, and constitutive rules are implemented for the creation and annihilation of dislocations. A novel criterion is introduced according to which the properties are projected into the two-dimensional (2D) domain of simulation. The question is addressed whether it is allowed to neglect accelerations, as is done in simulations at lower deformation rates.

Keywords: High-speed dislocations; Discrete dislocation plasticity; Projection 3D; Computer methodology; High strain rate

1. Introduction

This paper extends a methodology for simulations of dislocation motion and the interactions of the moving dislocation with microstructural features within a single grain. This work is motivated by an interest in the role of dislocations during certain manufacturing operations that involve rather localized shearing at very high strain rates. In such cases, the dislocations may reach velocities close to the shear wave speed, which requires due modifications compared to existing discrete dislocation simulations. At least in a first approximation, the shearing deformations can be studied in a two-dimensional (2D) setting, involving (straight) edge dislocations. This requires a mapping of the actual 3D properties into the 2D domain, which has not received much attention, so far.

To make the approach more specific, we will focus on a particular 2D simulation of periodic cell in a long single crystal with the primary slip system oriented for easy glide. Following the approach of Van der

* Corresponding author. Tel.: +1-31-50-363-4898; fax: +1-31-50-363-4881.
E-mail address: hossonj@phys.rug.nl (J.Th.M. De Hosson).

0927-0256/01/$ - see front matter
PII: S0927-0256(00)00117-8

Giessen and Needleman in 1995 [1,2], the method departs (Section 2) from the stress and displacement fields surrounding a straight dislocation moving at high velocities in an elastic isotropic *infinite* medium. For high dislocation velocities these are given by Hirth and Lothe [3] and Weertman [4], who built on earlier work by Eshelby [5] and Frank [6]. The image fields that account for the boundary conditions are obtained from a finite element solution. The time integration associated with dislocation velocities and accelerations are briefly discussed in Section 3. Section 4 describes an approach to map the properties of the obstacles in the two-dimensions, depending on the type of interaction between obstacles and dislocation line. In Section 5 this criterion is applied to specific obstacle types.

2. Discrete dislocation plasticity

Consider an infinitely straight edge dislocation i moving at a *constant* velocity v^i in the x_1-direction of a (x_1, x_2, x_3) Cartesian laboratory reference frame. The dislocation line lies parallel to the x_3-axis and its Burgers vector of magnitude b^i along the positive or negative x_1-direction. Introducing the longitudinal wave velocity a_1 and the shear wave velocity a_2, according to

$$a_1 = \sqrt{\frac{\lambda + 2\mu}{\rho}} \quad \text{and} \quad a_2 = \sqrt{\frac{\mu}{\rho}}, \tag{1}$$

respectively, where λ and μ denote the Lamé elastic constants and ρ is the material density, and defining

$$\alpha^i = \sqrt{1 - \frac{v^{i2}}{2a_2^2}}, \quad \beta_1^i = \sqrt{1 - \frac{v^{i2}}{a_1^2}} \quad \text{and} \quad \beta_2^i = \sqrt{1 - \frac{v^{i2}}{a_2^2}}, \tag{2}$$

we can write the high-velocity displacement fields u_1^i and u_2^i of dislocation i as [4]

$$u_1^i\left(\Delta x_1^i, \Delta x_2^i\right) = \frac{b^i}{\pi}\frac{a_2^2}{v^{i2}}\left\{\arctan\left(\frac{\beta_1^i \Delta x_2^i}{\Delta x_1^i}\right) - \alpha^{i2}\arctan\left(\frac{\beta_2^i \Delta x_2^i}{\Delta x_1^i}\right)\right\}, \tag{3}$$

$$u_2^i\left(\Delta x_1^i, \Delta x_2^i\right) = \frac{b^i}{2\pi}\frac{a_2^2}{v^{i2}}\left\{\beta_1^i \ln\left(\left(\Delta x_1^i\right)^2 + \left(\beta_1^i \Delta x_2^i\right)^2\right) - \frac{\alpha^{i2}}{\beta_2^i}\ln\left(\left(\Delta x_1^i\right)^2 + \left(\beta_2^i \Delta x_2^i\right)^2\right)\right\} \tag{4}$$

with $(\Delta x_1^i, \Delta x_2^i) \equiv (x_1 - x_1^i(t), x_2 - x_2^i(t))$. The corresponding stresses are given by

$$\sigma_{12}^i\left(\Delta x_1^i, \Delta x_2^i\right) = \frac{2\mu b^i}{\pi}\frac{a_2^2}{\beta_2^i v^{i2}}\left\{\frac{\beta_1^i \beta_2^i \Delta x_1^i}{\left(\Delta x_1^i\right)^2 + \left(\beta_1^i \Delta x_2^i\right)^2} - \frac{\alpha^{i4}\Delta x_1^i}{\left(\Delta x_1^i\right)^2 + \left(\beta_2^i \Delta x_2^i\right)^2}\right\}, \tag{5}$$

$$\sigma_{11}^i\left(\Delta x_1^i, \Delta x_2^i\right) = \frac{2\mu b^i}{\pi}\frac{a_2^2}{v^{i2}}\left\{\frac{-\beta_1^i\left(\beta_2^{i2} + 1 - \alpha^{i2}\right)\Delta x_2^i}{\left(\Delta x_1^i\right)^2 + \left(\beta_1^i \Delta x_2^i\right)^2} + \frac{\alpha^{i2}\beta_2^i \Delta x_2^i}{\left(\Delta x_1^i\right)^2 + \left(\beta_2^i \Delta x_2^i\right)^2}\right\}, \tag{6}$$

$$\sigma_{22}^i\left(\Delta x_1^i, \Delta x_2^i\right) = \frac{2\mu b^i}{\pi}\frac{\alpha^{i2}a_2^2}{v^{i2}}\left\{\frac{\beta_1^i \Delta x_2^i}{\left(\Delta x_1^i\right)^2 + \left(\beta_1^i \Delta x_2^i\right)^2} - \frac{\beta_2^i \Delta x_2^i}{\left(\Delta x_1^i\right)^2 + \left(\beta_2^i \Delta x_2^i\right)^2}\right\}, \tag{7}$$

$$\sigma_{33}^i\left(\Delta x_1^i, \Delta x_2^i\right) = \nu\left(\sigma_{11}^i\left(\Delta x_1^i, \Delta x_2^i\right) + \sigma_{22}^i\left(\Delta x_1^i, \Delta x_2^i\right)\right), \tag{8}$$

where $\nu = 1/2\lambda/(\lambda + \mu)$ is Poisson's ratio. Both the stress fields and displacement fields contain the longitudinal wave velocity as well as the shear wave velocity through β_1^i and β_2^i, respectively.

The displacement fields (3) and (4) are the sums of two "dislocation type" fields. These were introduced by Weertman [4] so as to ensure that no externally applied force in the x_2-direction is required at the core of the dislocation in order to avoid infinite stresses in the limit $\Delta x_1^i = \Delta x_2^i = 0$.

The stress fields are valid for dislocations in an *infinite* elastic body. In the case of a *finite* body or sample, these fields will not comply with the boundary conditions (in terms of prescribed displacements or tractions as function of time). Therefore, a correction is necessary that traditionally is interpreted in terms of image dislocations. In 1995, Van der Giessen and Needleman [1] proposed to handle this correction by a finite element procedure instead. This leads to a decomposition of the problem in two fields denoted by ($\sim$) and ($\hat{}$), as illustrated in Fig. 1. The final fields of stress and displacement are then found as

$$\begin{aligned} u_j &= \tilde{u}_j + \hat{u}_j, \qquad \tilde{u}_j = \sum_i \tilde{u}_j^i \\ \sigma_{jk} &= \tilde{\sigma}_{jk} + \hat{\sigma}_{jk}, \quad \tilde{\sigma}_{jk} = \sum_i \tilde{\sigma}_{jk}^i \quad \text{with } j,k \in \{1,2\}. \end{aligned} \tag{9}$$

with the ($\hat{}$) fields obtained from a finite element solution.

As mentioned before, we focus in particular on simulations of a single crystalline strip of height $2h$ subjected to shear. Within this strip we assume a periodic microstructure with a periodicity of $2w$, so that we can confine attention to a cell of width $\times$ height $= 2w \times 2h$, as depicted in Fig. 2. Periodic boundary conditions apply in the x_1-direction. This periodicity can be enforced by the ($\hat{}$) fields, but it is more accurate to incorporate the periodicity of the dislocation distribution analytically. Referring to Refs. [1,2] for details, this is done by considering a string i of dislocations formed by the dislocation i and all its replicas in the periodic boxes. Analytical summation over all replicas (each at a distance $2w$ apart, see Fig. 2) in the x_1-direction yields the fields of the string of dislocations. Following the procedure we find

$$\begin{aligned} \tilde{u}_1^i(\Delta\xi_1^i, \Delta\xi_2^i) = {} & \frac{b^i a_2^2}{\pi v^{i^2}} \left\{ -\arctan\left[\frac{\tan\left(\frac{\pi}{2}\Delta\xi_1^i\right)}{\tanh\left(\frac{\pi}{2}\beta_1^i\Delta\xi_2^i\right)}\right] + \alpha^{i^2}\arctan\left[\frac{\tan\left(\frac{\pi}{2}\Delta\xi_1^i\right)}{\tanh\left(\frac{\pi}{2}\beta_2^i\Delta\xi_2^i\right)}\right]\right\} \\ & - \delta^i \frac{b^{i^2} a_2^2}{v^{i^2}}\left(\alpha^{i^2} - 1\right)\operatorname{sgn}\left(\Delta\xi_2^i\right), \end{aligned} \tag{10}$$

$$\tilde{u}_2^i(\Delta\xi_1^i, \Delta\xi_2^i) = \frac{b^i a_2^2}{2\pi v^{i^2}} \left\{ \beta_1^i \ln\left(\cosh\left(\pi\beta_1^i\Delta\xi_2^i\right) - \cos\left(\pi\Delta\xi_1^i\right)\right) - \frac{\alpha^{i^2}}{\beta_2^i}\ln\left(\cosh\left(\pi\beta_2^i\Delta\xi_2^i\right) - \cos\left(\pi\Delta\xi_1^i\right)\right)\right\} \tag{11}$$

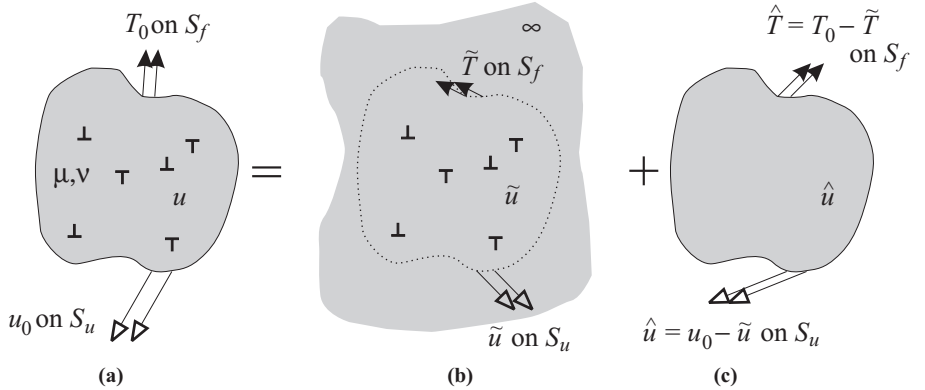

Fig. 1. (After Van der Giessen and Needleman [1]) Separation of (a) the total field into (b) the field ($\sim$) due to all dislocations in an infinite medium and (c) the complementary field ($\hat{}$) to correct for the boundaries. The mixed boundary conditions are the tractions T_0 on the surface S_f and displacements u_0 on the surface S_u.

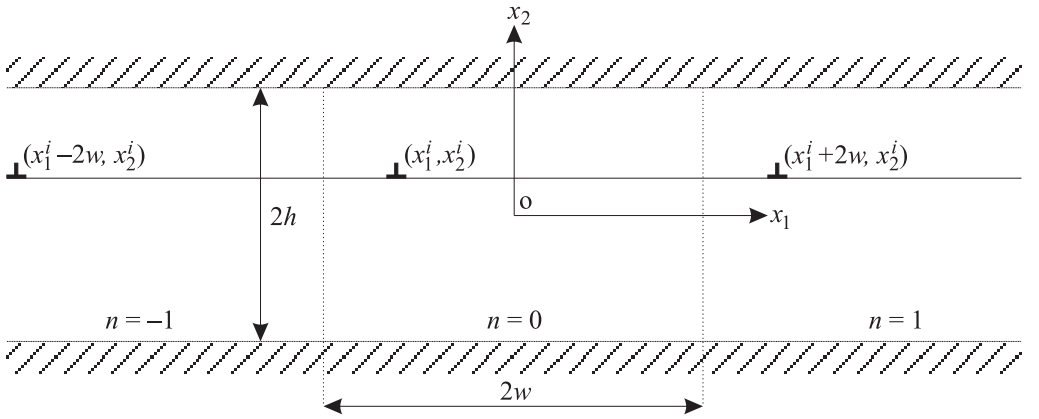

Fig. 2. The computational cell ($n=0$) of width × height $= 2w \times 2h$ containing dislocation i at (x_1^i, x_2^i). Replicas of dislocation i are shown in the periodic neighbouring cells $n=-1$ and $n=1$.

with $(\Delta\xi_1^i, \Delta\xi_2^i) \equiv (\Delta x_1^i/w, \Delta x_1^i/w)$ and

$$\delta^i = \begin{cases} -1 & \text{if} \quad \Delta\xi_1^i \in (-3/2, -1/2), \\ +1 & \quad\ \ \Delta\xi_1^i \in (+1/2, +3/2). \end{cases} \tag{12}$$

The term containing δ^i arises from the discontinuity in u_1 when a dislocation leaves the computational cell at one side and enters at the opposite site. This discontinuity arises from the fact that the arctan-function is multi-valued. The corresponding stress fields are found to be:

$$\tilde{\sigma}_{12}^i(\Delta\xi_1^i, \Delta\xi_2^i) = \frac{\mu b^i}{w}\frac{a_2^2}{\beta_2^i v^{i2}}\left\{\frac{\beta_1^i\beta_2^i \sin(\pi\Delta\xi_1^i)}{\cosh(\pi\beta_1^i\Delta\xi_2^i) - \cos(\pi\Delta\xi_1^i)} - \frac{\alpha^{i4}\sin(\pi\Delta\xi_1^i)}{\cosh(\pi\beta_2^i\Delta\xi_2^i) - \cos(\pi\Delta\xi_1^i)}\right\}, \tag{13}$$

$$\tilde{\sigma}_{11}^i(\Delta\xi_1^i, \Delta\xi_2^i) = \frac{\mu b^i}{w}\frac{a_2^2}{v^{i2}}\left\{\frac{-\left(\beta_1^{i2} + 1 - \alpha^{i2}\right)\sinh(\pi\beta_1^i\Delta\xi_2^i)}{\cosh(\pi\beta_1^i\Delta\xi_2^i) - \cos(\pi\Delta\xi_1^i)} + \frac{\alpha^{i2}\sinh(\pi\beta_2^i\Delta\xi_2^i)}{\cosh(\pi\beta_2^i\Delta\xi_2^i) - \cos(\pi\Delta\xi_1^i)}\right\}, \tag{14}$$

$$\tilde{\sigma}_{22}^i(\Delta\xi_1^i, \Delta\xi_2^i) = \frac{\mu b^i}{w}\frac{a_2^2\alpha^{i2}}{v^{i2}}\left\{\frac{\sinh(\pi\beta_1^i\Delta\xi_2^i)}{\cosh(\pi\beta_1^i\Delta\xi_2^i) - \cos(\pi\Delta\xi_1^i)} - \frac{\sinh(\pi\beta_2^i\Delta\xi_2^i)}{\cosh(\pi\beta_2^i\Delta\xi_2^i) - \cos(\pi\Delta\xi_1^i)}\right\}, \tag{15}$$

which reduce to the static form of [1] when $v^i/a_2 \to 0$. The shear stress $\tilde{\sigma}_{12}^i$ produced by a dislocation i with all its replicas is shown at different velocities in Fig. 3. As the velocity of the dislocation increases towards the shear wave speed a_2, the stress field changes drastically. In fact, at the Rayleigh velocity v_R, i.e. the velocity for which [3,4]

$$\beta_1^i\beta_2^i - \alpha^{i4} = 0 \tag{16}$$

the value of the shear stress $\tilde{\sigma}_{12}^i$ at the slip plane changes sign.

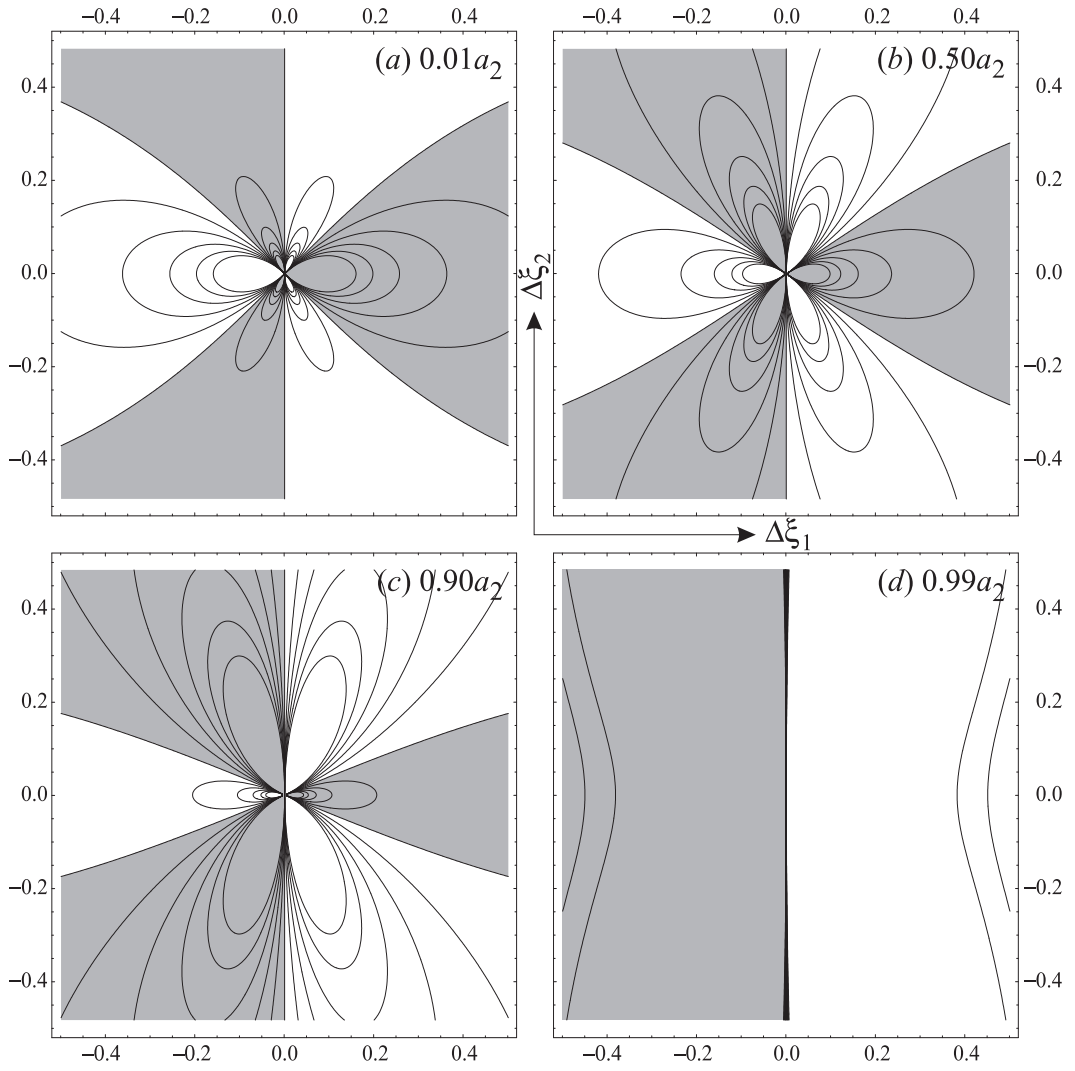

Fig. 3. Velocity dependence of the shear stress field $\tilde{\sigma}^i_{12}$ (Eq. (5)) of a positive edge dislocation i with all its replicas in a periodic cell of $2h = 2w = 2$ μm. The stress field is plotted for $-\mu/2000 < \tilde{\sigma}^i_{12} < \mu/2000$ in a region of 1.0×1.0 μm. The dislocation core is located at the origin. The number of contour lines is 11 over the entire range. The shading indicates a *positive* stress. The dislocation is moving in the positive x_1-direction with velocity (a) $v^i/a_2 = 0.01$ (b) $v^i/a_2 = 0.80$ (c) $v^i/a_2 = 0.90$ ($= v_R/a_2$ for $v = 1/3$), (d) $v^i/a_2 = 0.99$. The material properties have the values corresponding to Al.

3. Time integration

In studies on dislocation dynamics at low to intermediate strain rates [1,2,7], the inertial forces (i.e. accelerations) were neglected. In those cases, the dislocation attains its steady-state velocity in a time that is small compared to the typical length of a time increment. In the case of fast-moving dislocations, this may no longer be the case. In this section, both points of view will be developed and compared.

The Peach–Köhler force felt by dislocation i is a result of the combined stress-fields of all other dislocations j, and the "image" stresses $\hat{\sigma}_{ij}$. The long-range stresses of certain types of obstacles possibly also

contribute, but for now, we neglect the latter. The contribution to the Peach–Köhler force on dislocation i exerted by dislocation j in an infinite medium is

$$F^{j\to i}_{\text{Peach–Köhler}} = b^i \sigma^j_{12}\left(x^i_1 - x^j_1, x^i_2 - x^j_2\right). \tag{17}$$

The accumulated effect of all dislocations on the Peach–Köhler force at dislocation i is obtained by summation of the previous equation over all i. Thus, the total Peach–Köhler force on dislocation i, including the image contribution, is

$$F^i_{\text{Peach–Köhler}} = b^i\left(\hat{\sigma}_{12} + \sum_{j\neq i}\tilde{\sigma}^j_{12}\right). \tag{18}$$

It is of interest to note [4] that, due to the velocity dependence of the resolved shear stress, the magnitude of the force $F^{i\to j}$ is not necessarily equal to $F^{j\to i}$ (only when $v^i = \pm v^j$)! The two are equal, however, in the limit of v^i and v^j becoming much smaller than a_2.

The equation of motion for all dislocations is integrated in discrete time increments k of duration $\Delta t_k \equiv t_{k+1} - t_k$. Starting from a random initial distribution ($k = 0$) of dislocations in the computational cell, the velocities v^i_k during time increment k are calculated due to the combined forces on the dislocations at the start of the time increment. Note that a *random* configuration of dislocations is not necessarily an *equilibrium* configuration in terms of mechanical equilibrium.

First, we treat the case in which the accelerations are neglected (i.e. velocities are assumed to be attained instantaneously). The velocities v^i_k are constant during the time increment. From v^i_k and the positions (x^i_1, x^i_2) at the start of the time increment k, the positions of all dislocations at time increment $k+1$ can be calculated. Putting all the pieces together into Eq. (18) allows for writing an expression for the dislocation velocities v^i_k at time increment k due to all applied forces. Initially, $v^i_0 = 0$ for all i. For $k > 0$ and for all i, the velocities are given by the implicit relation

$$b^i\left(\hat{\sigma}_{12} + \sum_{j\neq i}\tilde{\sigma}^j_{12}\right)\Bigg|_k - B_{\text{TOT}}\left(v^i_k\right)v^i_k = 0, \tag{19}$$

where B_{TOT} denotes the drag coefficient, which may depend on the dislocation velocities v^i_k [8].

When inertial forces are included, the accelerations $\dot{v}^i_k$ are assumed to be constants during the time increment. Again using $v^i_0 = 0$ for all i, the accelerations are given by the solution of

$$b^i\left(\hat{\sigma}_{12} + \sum_{j\neq i}\tilde{\sigma}^j_{12}\right)\Bigg|_k - B_{\text{TOT}}\left(v^i_k\right)v^i_k = m_{\text{e}}\left(v^i_k\right)\dot{v}^i_k \tag{20}$$

(of which Eq. (19) is a special case). The velocity-dependent mass m_{e} is given by Hirth et al. [9] to be

$$m_{\text{e}}(v^i) = m_{\text{s},0}\left(\frac{a_2}{v^i}\right)^4\left(-8\beta^i_1 - \frac{20}{\beta^i_1} + \frac{4}{\beta^{i3}_1} + 7\beta^i_2 + \frac{25}{\beta^i_2} - \frac{11}{\beta^{i3}_2} + \frac{3}{\beta^{i5}_2}\right) \tag{21}$$

with

$$m_{\text{s},0} = \frac{\mu b^{i2}}{4\pi a_2^2}\ln\left(\frac{R}{r_0}\right) = \frac{\rho b^{i2}}{4\pi}\ln\left(\frac{R}{r_0}\right) \tag{22}$$

the "rest mass" of a screw dislocation. Usually, the cut-off radii R and r_0 are chosen such that $m_{\text{s},0} \cong \rho b_2$.

The velocities at the end of the time increment are found from

$$v^i_{k+1} = v^i_k + \dot{v}^i_k \Delta t_k \tag{23}$$

and the horizontal positions become

$$x^i_{1,k+1} = x^i_{1,k} + v^i_k \Delta t_k + \frac{1}{2} \dot{v}^i_k \Delta t^2_k. \tag{24}$$

When the velocity-dependence of $B_{\mathrm{TOT}}(v^i)$ is known, an estimate can be made of the typical time needed for a dislocation to reach the velocity it would be given in the approach without acceleration.

4. Constitutive rules

Several forces act on the dislocation to drive it to its velocity. The equation of motion of the dislocations, as described in Section 3, can be integrated in time as long as obstacles do not hinder the motion. Obstacles trap dislocations, new dislocations are generated during deformation and dislocations of opposite sign annihilate upon meeting each other.

The method of discrete dislocation plasticity takes these events into account in an easy manner [1,2]. For instance, if at a certain instant the distance between two dislocations of opposite sign on the same slip plane is less than a pre-set value $L_{\mathrm{annihilate}}$, their mutual attraction becomes so high that they will collide and annihilate each other (i.e. they will be removed from the slip plane). The value of $L_{\mathrm{annihilate}}$ is typically of the order of a few lengths b^i of the Burgers vector. In the next two sections, discrete obstacles and generation of dislocation will be considered.

Some characteristic quantities pertaining to discrete obstacles in the slip plane are depicted in Fig. 4. Here L^i_{obs} denotes the size or range of interaction of obstacle i in the slip plane in the direction of slip (the x_1-direction of the computational cell), z^i_{obs} the size of obstacle i in the slip plane perpendicular to the direction of slip (the x_3-direction in the computational cell) and Λ the mean obstacle spacing.

There are several physical mechanisms limiting dislocation motion. For instance, the dislocation may find solute atoms, precipitates or forest dislocations in its slip plane. While crossing unit distance, the dislocation spends a time t_{wait} waiting to pass these obstacles and a time t_{move} moving from one obstacle to the next. In the regime where $t_{\mathrm{wait}} \gg t_{\mathrm{move}}$ the dislocation is said to undergo *jerky glide*. The dislocation spends almost all of its time waiting to pass some obstacle. The dislocation may pass an obstacle by cutting through, or bowing around it. The process offering the lowest resisting force determines the strength of the obstacle. The energy spent in the process can be supplied by an increase of the Peach–Köhler force, or by thermal fluctuations. Above a certain threshold of the force or temperature, the obstacles no longer impede dislocation motion. In this *drag-controlled regime* (or *viscous flow*), for which $t_{\mathrm{move}} \gg t_{\mathrm{wait}}$, the dislocations loose energy mainly by interaction with phonons and electrons.

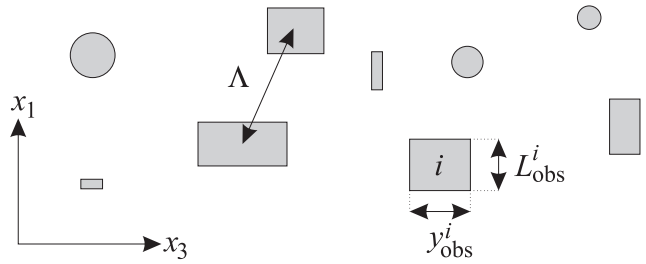

Fig. 4. Top view of the slip plane with some obstacle parameters. Here L^i_{obs} denotes the size or range of interaction of obstacle i in the direction of slip, z^i_{obs} the size of obstacle i in the slip plane perpendicular to the direction of slip and Λ the mean obstacle spacing. Note also the different *types* of obstacles present, each with a different value for Λ.

This section focuses on the regime of jerky glide. This implies that we interpret the flow stress as the stress required to overcome the obstacles *only*. The effects of thermal activation are excluded i.e., the temperature is assumed to be 0 K.

4.1. Mapping of obstacle properties into 2D

The properties of obstacles have to be mapped from the 3D crystal into the 2D representation (Fig. 5). The initial configuration may contain several types of obstacles distributed randomly across the slip planes. The parameters available in two dimensions are the effective average obstacle strength ι_{eff}, the effective obstacle spacing l_{eff}, the effective size L_{eff} of the cross-section of obstacles in the slip plane and the effective waiting time t_{eff}. It is also possible to include obstacles having long-range stress fields. The parameters in the 2D cell have to represent parameters from the 3D crystal: the obstacle spacing Λ, the line tension of the dislocation line, the number of obstacles interacting with the dislocation line, the average obstacle size L_{obs} and the obstacle strength τ_{obs}.

Some special care has to be taken when discussing obstacle spacings and fractions. For instance for solutes, when the sample contains an atomic fraction c of solutes, some average distances can be defined, depending on the dimensionality of the distribution that is under consideration. In three dimensions, the average distance λ_3 between the centers of the obstacles is $b/c^{1/3}$. When a plane cuts the volume, the average distance λ_2 between obstacle centers in the plane is $b/c^{1/2}$. When the volume is cut by a line, the average spacing λ_1 along the line is b/c.

In our case, the normal of the plane of the computational cell points in the x_3-direction. The slip planes on which the edge dislocations move cut this plane perpendicularly, resulting in lines along the x_1-direction. The obstacle spacing along the line representing the slip plane is then λ_1. Equivalently, the *straight* dislocation line, which lies along the x_3-direction, meets $1/\lambda_1 = c/b$ obstacles per unit length.

The idea is now that an analysis of the processes by which the dislocation line passes the obstacles yields the effective jump distance l_{eff}, the activated length of dislocation line and the number of obstacles n along the activated length, for each type of interaction. The obstacle strength can be estimated from experimental data to be the flow stress for a grain of a particular material. When the contributions from each type of obstacle can be identified from the experimental data (for instance as in [10,11]), or when only one type of

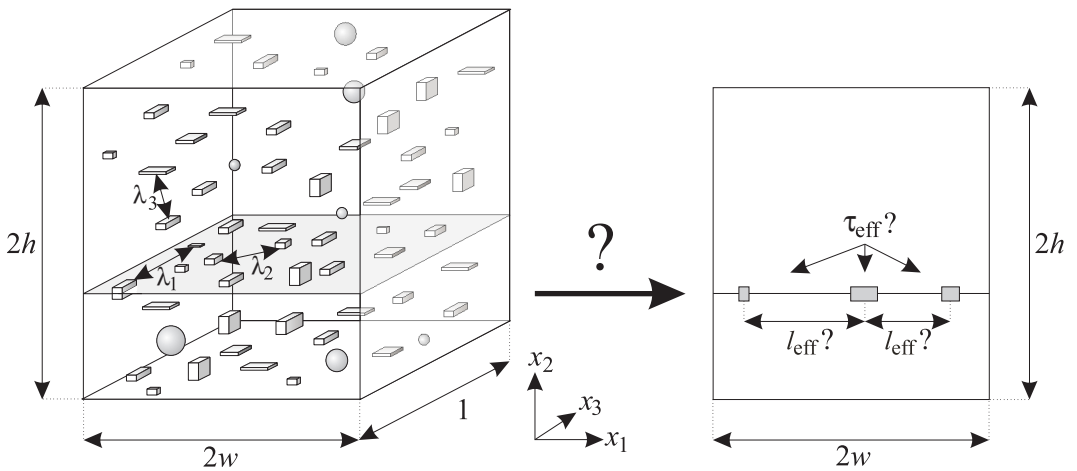

Fig. 5. Mapping of a 3D crystal into a 2D computational cell. Here λ_1 denotes the *linear* spacing, λ_2 the *planar* spacing and λ_3 the *volume* spacing.

obstacle contributes to the flow stress, the strength of a single obstacle can be calculated. Conversely, the values of the effective parameters are immediately reflected in the predicted flow stress that can be read off the simulated stress–strain curves in the regime of jerky glide.

The dislocation line overcomes obstacles either by cutting through or bowing around them. Each process is activated when the applied stress reaches a certain threshold. The process with the lowest threshold is the one that actually takes place. Fig. 6 displays the different manners in which a dislocation line interacts with obstacles. Obstacles that can be passed by cutting through are called *shearable* obstacles, or *penetrable* obstacles. When a dislocation bows around an obstacle, it is called a *non-shearable*, or an *impenetrable* obstacle. We first consider shearable obstacles and end with non-shearable obstacles.

Another division of obstacles is according to their interaction with the surrounding medium. Some obstacles have long-range elastic stress fields, such as the interaction between a dislocation and the stress fields of all the other dislocations. Obstacles giving rise to such long-range interactions are termed *diffuse obstacles*. Their interaction may be take into account *explicitly* within the framework of DDP, but even in that case, their interactions have to be described within a 2D setting. On the other hand, some obstacles interact only locally with the dislocation line. These obstacles are termed *localised* obstacles. Small coherent precipitates form an example.

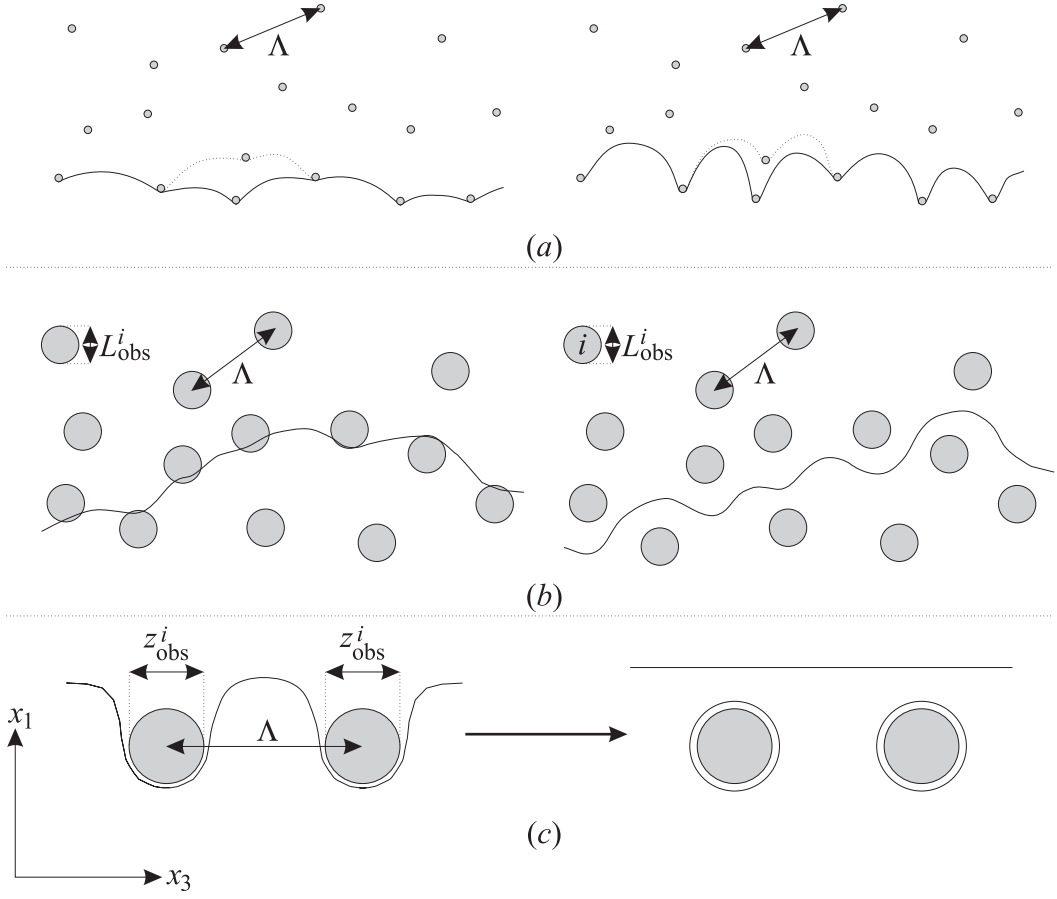

Fig. 6. Interaction of a dislocation line with obstacles: (a) the Friedel limit $\eta_0 < 0$. Left: weak interaction [13]. Right: strong interaction; (b) the Mott–Labusch limit $\eta_0 > 0$. Left: weak interaction. Right: strong interaction; (c) Orowan looping around non-shearable obstacles.

In real crystals, the dislocation lines are seldom straight. A further division is based on the ability of the obstacle to bend nearby parts of the dislocation through a large angle against the line tension T. Obstacles with that ability are *strong obstacles*, whereas those without are *weak obstacles*. The last two criteria are combined in the dimensionless Labusch-parameter [12,13]

$$\eta_0 = \frac{L_{\text{obs}}}{\Lambda}\sqrt{\frac{2T}{F_{\max}}}, \tag{25}$$

where $F_{\max}$ denotes the maximum applied force that the obstacle can resist. This parameter consists of two dimensionless parameters (L_{obs}/Λ) and ($F_{\max}/2T$).

4.1.1. Friedel limit

When $\eta_0 \leqslant 1$, the interaction of the dislocation line with the obstacle takes place over a small segment. The interaction is then considered to be a point force. The interaction between dislocation line and localized obstacle may bend the dislocation line over a *cusp angle* φ against the line tension $T \approx 1/2\mu b^2$. At the critical breakaway angle φ_c, which occurs at the maximum applied force which the obstacle can resist, $F = F_{\max}$. The critical breakaway angle is used as a normalized measure for the obstacle strength:

$$\cos(\varphi_c) = \frac{F_{\max}}{2T} = \frac{F_{\max}}{\mu b^2} \equiv f_c. \tag{26}$$

Each obstacle resists the forward force τbl on a segment of line of initial length l and at the maximum $F_{\max}$,

$$\tau_{\max} = \frac{F_{\max}}{bl} = \frac{\mu b}{l} f_c. \tag{27}$$

The number of obstacles per unit length in contact with the dislocation line depends on the curvature of the line. This in turn depends on the force on the line. When the line is slightly curved, the length per obstacle is the Friedel length [14]:

$$l_F = \frac{\Lambda}{\cos(\varphi_c)^{1/2}} = \frac{\Lambda}{f_c^{1/2}} \tag{28}$$

leading to an effective obstacle strength of

$$\tau_{\max,\ \text{Friedel}} \equiv \tau_F = \frac{\mu b}{l_F} f_c = \frac{\mu b}{\Lambda} f_c^{3/2} \tag{29}$$

In the derivation of this length, the assumptions are made that the dislocation line advances by unpinning of one obstacle at a time, thereby covering an area of Λ^2, the average area per obstacle.

The transition to an effective jump length can now be made as follows. When a dislocation jumps, it covers an area of Λ^2. From the derivation of the Friedel length, we consider a depth of $2l_F$. Our "effective" straight dislocation should cover the same area, or $\Lambda^2 = 2l_F l_F^{\text{eff}}$, leading to (Fig. 7)

$$l_F^{\text{eff}} = \frac{\Lambda^2}{2l_F} = \frac{\Lambda\sqrt{f_c}}{2} \tag{30}$$

the effective spacing for Friedel obstacles in 2D. The jump of the dislocation should occur at the same Peach–Köhler force in the 2D and in the 3D case. Since the Friedel stress is derived for the jump over one obstacle at the time, each *effective* obstacle has a strength $\tau_F^{\text{eff}} = \tau_F$.

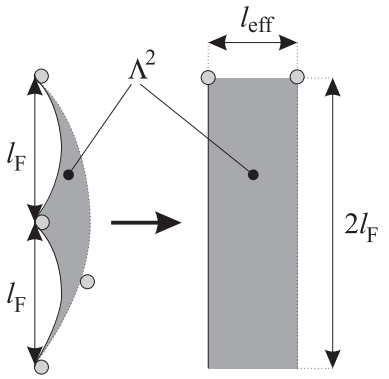

Fig. 7. Slip area in the Friedel approximation and its projection into an effective straight dislocation.

4.2. Mott–Labusch limit

When $\eta_0 \gtrsim 1$, *diffuse* obstacles are assumed to create an average stress τ_i in a region of size Λ, the average obstacle spacing (Fig. 6(b)). The diffuse forces again bend the dislocation line into an arc of radius R against the line tension T. When $R \lesssim \Lambda$, the interaction is called *strong* (left Fig. 6(b)), and *weak* for $R \gg \Lambda$ (right Fig. 6(b)).

For weak obstacles, the realm of the Mott–Labusch description is entered. The physical picture given by Nabarro underlying the Labusch derivation is that of a mean fluctuation in the sign of the obstacle interaction, whereas in the Friedel picture, all obstacles are repulsive. The dislocation line advances by unpinning at several obstacles at a time over the length l_{M}. The number of obstacles is given by [13,15]

$$n = \left(\frac{2T}{F_{\max}}\frac{L_{\mathrm{obs}}^2}{\Lambda^2}\right)^{2/3} = \eta_0^{4/3} = \left(\frac{L_{\mathrm{obs}}}{\Lambda\sqrt{f_{\mathrm{c}}}}\right)^{4/3} \tag{31}$$

and the obstacle strength can be written as

$$\tau_{\max,\ \text{Mott–Labusch}} = \tau_{\mathrm{M}} = \left(\frac{2}{\pi}\right)^{3/2}\frac{\mu b}{l} f_{\mathrm{c}}^{3/2} n^{1/4} \equiv \frac{\mu b}{l_{\mathrm{M}}}\bar{f}_{\mathrm{c}}. \tag{32}$$

Here $\bar{f}_{\mathrm{c}}$ denotes the *average* stress $(2/\pi) f_{\mathrm{c}}$ and l_{M} has been defined so that the right-hand side takes the same form as (30). It follows that

$$l_{\mathrm{M}} = \frac{\Lambda}{n^{1/4}\bar{f}_{\mathrm{c}}^{1/2}} = \sqrt{\frac{\pi}{2}}\frac{l_{\mathrm{F}}}{\eta_0^{1/3}} = \sqrt{\frac{\pi}{2}}\left(\frac{\Lambda^4}{L_{\mathrm{obs}} f_{\mathrm{c}}}\right)^{1/3}. \tag{33}$$

The transition of a 3D crystal to the 2D model can now be made in a similar fashion as was done for Friedel-like obstacles. In Fig. 8, the slip area is estimated. Here the assumption is made that the curved boundary of the area of slip can be approximated by a parabola [14], with a maximum departure from the straight boundary of Λ. In that case, the area is given by $2/3\Lambda l_{\mathrm{M}}^{\mathrm{eff}}$ and the effective length becomes

$$l_{\mathrm{M}}^{\mathrm{eff}} = \frac{2}{3}\Lambda. \tag{34}$$

The strength of the effective obstacle becomes the Mott flow stress τ_{M} (Eq. (32)), since it represents the resistance to flow due to the fluctuations of the interaction force of all n obstacles along the Mott length.

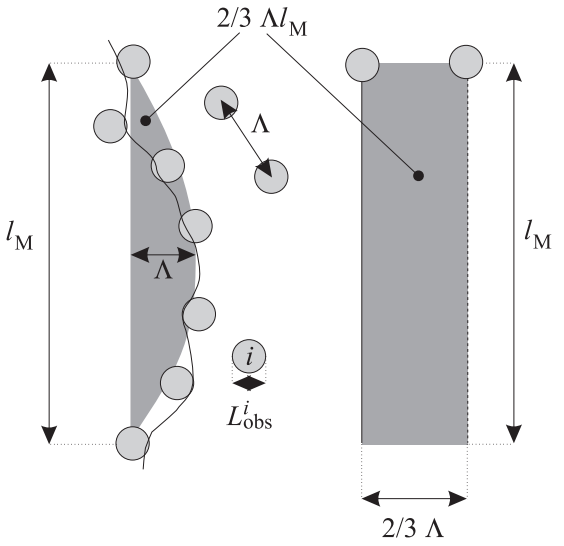

Fig. 8. Projection of Mott–Labusch obstacles into the 2D model.

For strong diffuse obstacles, the radii of the arcs into which the dislocation line is bent are of the order of the obstacle spacing Λ, so that $l_M \cong \Lambda$. The flow stress is that required to overcome the mean internal stress [16] $\bar{\tau} = \bar{F}/bL_{obs}$, where $\bar{F}$ denotes the average Peach–Köhler force due to the interaction between the dislocation line and the obstacles. This can be seen by setting $L_{obs} \cong \Lambda$, so that on the one hand the mean internal stress becomes $\bar{\tau} \cong \bar{F}/b\Lambda$, and on the other hand, using Eqs. (26) and (32),

$$\tau_{\text{max, Mott–Labusch, strong}} = \sqrt{\frac{\pi}{2}}\frac{\mu b}{l_M}\bar{f}_c \cong \sqrt{\frac{\pi}{2}}\frac{\bar{F}}{b\Lambda} \cong \bar{\tau}. \tag{35}$$

4.2.1. Orowan looping

When the obstacle is non-shearable, the dislocation line may pass the obstacle by bowing around it. This process is known as the Orowan mechanism (Fig. 6(c)). The two parts of the dislocation line on either side of the obstacle will attract and form a dipole. When they are close enough, the loop closes around the obstacle and the remaining part of the dislocation line is no longer bound by the obstacle. The resisting force is of the order of the line tension and $\cos(\varphi_c) \sim 1$, so Eq. (27) yields

$$\tau_{\text{Orowan}} \cong \frac{\mu b}{\Lambda}. \tag{36}$$

In this approach, no account has been taken of the self-stress due to the dipole orientation of the dislocation segments that are bent around the obstacle, or the size of the obstacle, which may be of the order of Λ. Taking this into account gives [17]

$$\tau_{\text{Orowan}} = \frac{0.84\mu b}{2\pi(1-\nu)}\frac{\ln\left(d^s_{obs}/r_0\right)}{\left(\Lambda - d^s_{obs}\right)}. \tag{37}$$

Here d^s_{obs} is the *mean* diameter of the spherical particles *in the plane*, which equals $(\pi/8)z_{obs}$, and r_0 denotes the core radius of the dislocation (typically $\sim b$). The factor 0.84 takes into account the fact that the

dislocation moves in areas where the obstacles are relatively widely spaced, thereby increasing the effective obstacle spacing [16].

The slip area per obstacle is Λ^2 (Fig. 6(c)). The original interaction length of the dislocation line is Λ, so the *effective* projected obstacle spacing l_O^{eff} also reduces to Λ.

4.3. Generation of dislocations

In real crystals, several mechanisms give rise to the creation of dislocations, such as the self-replicating process of a Frank–Read source, generation at grain boundaries, generation at stress concentrators, or through the double cross-slip process. The latter requires modelling in terms of screw dislocations.

According to [12], the sources, or nucleation sites i can be characterized by their intrinsic stress field $\sigma^i_{\text{nuc}}(\Delta x^i_1, \Delta x^i_2)$, the source diameter L^i_{nuc} and the source strength τ^i_{nuc}, above which dislocations will be generated at the boundaries of the source. The Δx^i_1 and Δx^i_2 are defined in the same manner as for dislocations. The intrinsic stress field of the source can take different forms. In this work, all sources are modeled after a Frank–Read source. It is a localized source with $\sigma^i_{\text{nuc}} = 0$ for all $|\Delta x^i_1|,\ |\Delta^i_2| > 1/2L^i_{\text{nuc}}$.

The source strength τ^i_{nuc} of a Frank–Read source is determined by the length in the x_3-direction, z^i_{nuc}, of the segment between its pinning points and the stress needed to bow out the segment against the line tension. It is given by

$$\tau^i_{\text{nuc}} = \frac{\mu b^i}{z^i_{\text{nuc}}}, \tag{38}$$

where b^i is the magnitude of the Burgers vector of the dislocation segment between the pinning points.

The length in the x_3-direction is a fraction of the initial density of forest dislocations ρ_F^{initial}, since these provide the pinning points for the dislocation segment. Introducing the proportionality factor f_N, this gives an average length between the pinning points:

$$z^i_{\text{nuc}} = \frac{1}{\sqrt{f_N \rho_F^{\text{initial}}}}. \tag{39}$$

The source diameter L^i_{nuc} and the source strength τ^i_{nuc} are related through the condition that the applied resolved shear stress balances the attraction between the freshly formed dislocation pair at $(\Delta x^i_1,\ \Delta x^i_2) = (\pm 1/2L^i_{\text{nuc}}, 0)$. This leads to

$$L^i_{\text{nuc}} = \frac{\mu}{2\pi(1-\nu)} \frac{b^i}{\tau^i_{\text{nuc}}} = \frac{\bar{z}^i_{\text{nuc}}}{2\pi(1-\nu)}. \tag{40}$$

For very small segment lengths z^i_{nuc} this only gives the order of magnitude, since the error in representing the cross-section of the loop by straight dislocation is largest for small loops.

At high strain rates, the rate at which dislocations are generated may be of crucial importance. The time needed by a dislocation segment to cross the source region is taken as the time needed to nucleate a dislocation loop. In this manner, the nucleation time is directly coupled to the effective stress on the source region and to its size, as is physically plausible.

The nucleation sites also manifest themselves as obstacles to dislocation motion. When a dislocation passes a source region, we assume that it has to bend around it, so its strength follows an Orowan-type equation (37). The size of the source in the x_3-direction again equals the length of the segment of dislocation line forming the Frank–Read source.

5. Obstacle properties

The Section 4.3 dealt with a manner in which properties of 3D crystals map onto the 2D domain (Fig. 2), and the various regimes dictating obstacle strengths and interaction lengths. In this section the theory is applied to actual obstacles present in the model crystal: solute atoms, forest dislocations and precipitates.

5.1. Solutes

Substitutional or interstitial solid solutions pose obstacles to dislocation motion of size L_{obs} on the order of b. Experimental studies by NMR- and TEM-techniques show that solutes interact with the dislocation line according to Mott–Labusch statistics [10]. Usually only the solutes directly above and below the slip plane are taken into account. In that case, Λ equals the in-plane spacing (see Fig. 5) $\lambda_2 = b/(2c)^{1/2}$ (the factor 2 in the denominator takes into account the two planes on either side of the slip plane). Substitution into Eqs. (31) and (34) yields

$$l_{\text{M}}^{\text{eff}} = \frac{b}{3}\sqrt{\frac{2}{c}} \tag{41}$$

and

$$n = \left(\frac{2c}{f_{\text{c}}}\right)^{2/3}. \tag{42}$$

Then the number of solutes on each slip plane of length $2w$ equals

$$\frac{2w}{l_{\text{M}}^{\text{eff}}} = \frac{6w}{b}\sqrt{\frac{c}{2}}. \tag{43}$$

The obstacle strength (Eq. (32)) becomes

$$\tau_{\text{obstacle}}^{\text{solute}} = \mu\left(\frac{2}{\pi}\right)^{3/2}\sqrt[3]{4c^2 f_{\text{c}}^4}. \tag{44}$$

5.2. Forest dislocations

The number of forest dislocations varies when the deformation activates secondary slip systems (i.e. the transition from stage I to stage II deformation). The dislocation lines of the secondary slip systems intersect the primary plane where they hinder the dislocation motion. The obstacle size is of the order of the size of the dislocation core, i.e. $L_{\text{obs}} \sim b$. The complicated interactions between the forest dislocations and the dislocations in the primary slip plane (the "primaries") due to their relative orientations are often modeled by a static collection of fixed and randomly distributed point obstacles [17]. In fact, the interaction between dislocation line and forest dislocations is shown experimentally to follow the Friedel statistics of localized obstacles [10].

The number of forest dislocations changes during the deformation due to dislocation generation and annihilation in the secondary slip systems. In the 2D computational cell this is captured by changing the number of obstacles on the slip planes. The density of forest dislocations ρ_{F} is assumed to be a fixed fraction f_{F} of the overall mobile dislocation density ρ_{M}. During stage II, the density of forest dislocations is of the same order of the density of the primaries, so $f_F \sim 1$. Here the assumption is made that the forest dislocations are distributed randomly throughout the crystal. Their planar spacing may then be taken as $\Lambda \cong \rho_{\text{F}}^{-1/2}$. Substitution into Eq. (29) leads to a Friedel length of

$$l_F = \frac{1}{\sqrt{\rho_F f_c}} = \frac{1}{\sqrt{f_F \rho_M f_c}}. \tag{45}$$

Using Eq. (31), the effective spacing l_F^{eff} becomes

$$l_F^{eff} = \frac{\Lambda\sqrt{f_c}}{2} = \frac{1}{2}\sqrt{\frac{f_c}{f_F \rho_M}}, \tag{46}$$

yielding

$$\frac{2w}{l_F^{eff}} = 4w\sqrt{\frac{f_F \rho_M}{f_c}} \tag{47}$$

forest dislocations on each slip plane of length $2w$. In the specific computational cell of Fig. 2, a new obstacle is placed at a random position at a randomly chosen slip plane whenever the integer value of $(2w/l_F^{eff})$ times the total number of slip planes increases by one. The effective obstacle strength (Eq. (29)) is

$$\tau_{obstacle}^{forest\ dislocation} = \mu b\sqrt{f_F \rho_M f_c^3}. \tag{48}$$

The obstacle strength f_c is determined by the value of the break-away angle $\varphi_c = \arccos(f_c)$ which has to be provided by experiments.

5.3. Precipitates

When a precipitate starts to grow from a solid solution, it may provide a long-range stress in the surrounding matrix due to elastic misfit. When coherency is lost, misfit dislocations capture the misfit at the interfaces, effectively eliminating the long-range stress field. A dislocation may pass a precipitate by either cutting through or bowing around it, depending on which process offers the least resistance. In the course of the fast deformation, the initial number of precipitates will not change, since the process time is far too small for that. The same holds for the ratio of coherent to incoherent precipitates.

The precipitates are considered to be spherical with a mean radius of R^p and occupying a volume fraction c_V in the crystal. When the precipitates have no long-range stress field, only the intersections of the precipitates with the slip plane pose as obstacles to dislocation motion. The mean spacing Λ then equals the *planar* spacing $\lambda_2 = (2\pi/3c_V)^{1/2}R^p$, and the mean obstacle size L_{obs} in the glide plane is $1/2\pi R^p$. On the other hand, when the long-range elastic interactions are taken into account, the mean spacing Λ becomes the *volume* spacing $\lambda_3 = (4\pi/3c_V)^{1/3}R^p$ (see Fig. 5) and the mean obstacle size $L_{obs} = 2R^p$.

In the case of incoherent precipitates, the equivalent obstacle spacing in two dimensions becomes, according to Eq. (30),

$$l_{F,\ eff}^{incoherent\ precipitates} = \sqrt{\frac{\pi f_c}{6c_V}}R^p. \tag{49}$$

and the effective obstacle strength (Eq. (29)) is

$$\tau_{obstacle}^{incoherent\ precipitates} = \frac{\mu b}{R^p}\sqrt{\frac{3c_V f_c^3}{2\pi}}. \tag{50}$$

In the case of coherent precipitates (involving long-range stress fields), Mott–Labusch statistics apply and the equivalent obstacle spacing (Eq. (34)) becomes

$$l_{\mathrm{M,\ eff}}^{\text{coherent precipitates}} = \frac{2}{3}\sqrt[3]{\frac{4\pi}{3c_{\mathrm{V}}}}R^{\mathrm{p}} \tag{51}$$

with (Eq. (31))

$$n = \left(\frac{3c_{\mathrm{V}}}{4\pi}\right)^{4/9}\left(\frac{4}{f_{\mathrm{c}}}\right)^{2/3} \tag{52}$$

interacting precipitates along the Mott length of dislocation line. The obstacle strength (Eq. (32)) reads

$$\tau_{\mathrm{obstacle}}^{\text{coherent precipitates}} = \frac{\mu b}{R^{\mathrm{p}}}\left(\frac{2}{\pi}\right)^{3/2}\sqrt[9]{\frac{81c_{\mathrm{V}}^4}{32\pi^4}}\sqrt[3]{f_{\mathrm{c}}^4}. \tag{53}$$

The dislocation line passes the incoherent precipitates either by cutting through (which is a short-range interaction) or by bowing around in an Orowan-process. In our simulations we choose the process with the lowest flow stress according to Eqs. (29) and (37). The sizes and concentrations of precipitates are specified during the generation of the initial configuration, so then the appropriate spacing along the slip plane can be selected.

Table 1 summarizes the quantities of interest in 2D simulations of the type considered here. It contains the effective lengths and effective obstacle strength that were derived above, and also the values for nucleation sites.

We conclude by showing, in Fig. 9, an example of the initial configuration of the computational cell of Fig. 2, including the slip planes, obstacles, nucleation sites and a random distribution of dislocations. The microscopic properties were chosen to give a clear figure rather than to reflect an actual simulation. In this case, the computational cell measured $2w \times 2h = 2 \times 2$ μm, the dislocations with an initial density of $5 \times 10^{1}3\ \mathrm{m}^{-2}$ are distributed randomly over 10 slip planes. The cell contains solutes with an atomic fraction $c = 5 \times 10^{-5}$, forest dislocations with a strength $f_{\mathrm{c}} = 4.3 \times 10^{-2}$ and a fixed fraction of the mobile dislocation density of $f_{\mathrm{F}} = 10^{-3}$, and coherent precipitates of mean radius $R^{\mathrm{p}} = 7.2$ nm and a volume concentration $c_{\mathrm{V}} = 10^{-4}$. Finally, the nucleation sites have a proportionality factor to the initial dislocation density

Table 1
Summary if the parameters characterzing effecting strengths and lengths in 2D domians

Obstacle type	Obstacle size L_{obs} (m)	Obstacle spacing Λ (m)	Effective obstacle spacing l_{eff} (m)	Effective obstacle strength τ_{eff} (Pa)
Solute atom	b	$\frac{b}{\sqrt{2c}}$	$\frac{b}{3}\sqrt{\frac{2}{c}}$	$\mu\left(\frac{2}{\pi}\right)^{3/2}\sqrt[3]{4c^2f_{\mathrm{c}}^4}$
Forest dislocation	b	$\frac{1}{\sqrt{f_{\mathrm{F}}\rho_{\mathrm{M}}}}$	$\frac{1}{2}\sqrt{\frac{f_{\mathrm{c}}}{f_{\mathrm{F}}\rho_{\mathrm{M}}}}$	$\mu b\sqrt{f_{\mathrm{F}}\rho_{\mathrm{M}}f_{\mathrm{c}}^3}$
Incoherent precipitate	$\frac{\pi}{2}R^{\mathrm{p}}$	$\sqrt{\frac{2\pi}{3c_{\mathrm{V}}}}R^{\mathrm{p}}$	$\sqrt{\frac{\pi f_{\mathrm{c}}}{6c_{\mathrm{V}}}}R^{\mathrm{p}}$	$\frac{\mu b}{R^{\mathrm{p}}}\sqrt{\frac{3c_{\mathrm{V}}f_{\mathrm{c}}^3}{2\pi}}$
Coherent precipitate	$2R^{\mathrm{p}}$	$\sqrt[3]{\frac{4\pi}{3c_{\mathrm{V}}}}R^{\mathrm{p}}$	$\frac{2}{3}\sqrt[3]{\frac{4\pi}{3c_{\mathrm{V}}}}R^{\mathrm{p}}$	$\frac{\mu b f_{\mathrm{c}}^{4/3}}{R^{\mathrm{p}}}\left(\frac{2}{\pi}\right)^{3/2}\sqrt[9]{\frac{81c_{\mathrm{V}}^4}{32\pi^4}}$
Impenetrable obstacle	$\frac{\pi}{2}R^{\mathrm{p}}$	$0.84\sqrt{\frac{2\pi}{3c_{\mathrm{V}}}}R^{\mathrm{p}}$	$0.84\sqrt{\frac{2\pi}{3c_{\mathrm{V}}}}R^{\mathrm{p}}$	$\frac{0.84\mu b}{2\pi(1-\nu)}\frac{\ln(L_{\mathrm{obs}}/b)}{\Lambda - L_{\mathrm{obs}}}$
Dislocation source	$\frac{1/2\pi}{(1-\nu)\sqrt{f_{\mathrm{N}}\rho_{\mathrm{F}}^{\mathrm{initial}}}}$	$\frac{0.84\sqrt{2}}{\sqrt{f_{\mathrm{N}}\rho_{\mathrm{F}}^{\mathrm{initial}}}}$	$\frac{0.84\sqrt{2}}{\sqrt{f_{\mathrm{N}}\rho_{\mathrm{F}}^{\mathrm{initial}}}}$	$\frac{0.84\mu b}{2\pi(1-\nu)}\frac{\ln(L_{\mathrm{obs}}/b)}{\Lambda - L_{\mathrm{obs}}}$

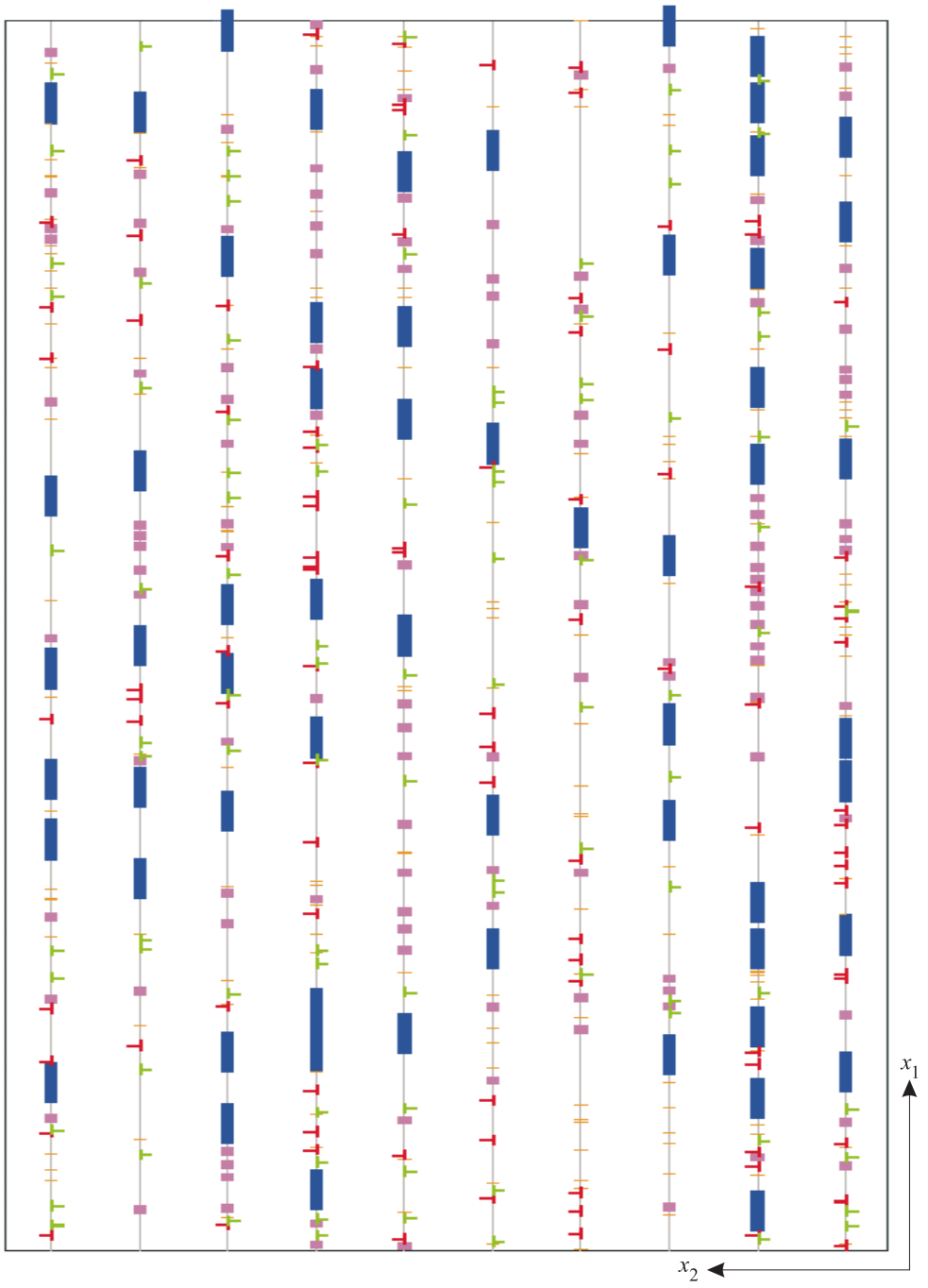

Fig. 9. Example of the initial configuration in the computational cell (rotated 90° and stretched in the x_1-direction). The computational cell of $2w \times 2h = 2 \times 2$ μm contains 10 horizontal slip planes (gray). The cell contains dislocations (positive: red and negative: green), nucleation sites (blue), precipitates (magenta) and solutes and forest dislocations (orange). The parameters that were used to generate this particular configuration are given in the text.

of $f_N = 0.25$. Note that the initial random configuration of dislocations is not necessarily in equilibrium with respect to the dislocation–dislocation interactions. Before applying the actual deformation history, the dislocation structure needs to be relaxed under the influence of the dislocation–dislocation interactions.

6. Summary

In this paper the basic ingredients have been introduced for simulations of dislocation dynamics at high strain rates. The first section introduced the stress and displacement fields of a straight, fast-moving edge dislocation in an infinite medium. However, we are interested in dislocations moving in a finite medium. In order to make the discussion specific, we have focussed on a 2D computational cell, which is periodic in the horizontal direction. This cell contains horizontal slip planes and represents a single slip system in an infinite strip of close-packed metal. Section 2 described the stresses and displacements in the computational cell, taking into account the boundaries of the cell. Section 3 explained the time integration, where two cases are considered, with or without acceleration.

Any crystal in the ''real world'' contains obstacles that may impede dislocation motion. These have to be projected into the 2D computational cell. In Section 4, a criterion is developed for this, based on a constant slip area per obstacle. This criterion depends on the type of interaction between the dislocation line and the obstacle. Section 5 applies this criterion to specific obstacles, leading to a set of projections as summarized in Table 1.

Acknowledgements

The work described in this paper is supported by IOP-metals under project number C94.703.RG.TF.

References

[1] E. Van der Giessen, A. Needleman, Discrete dislocation plasticity: a simple planar model, Modelling Simul. Mater. Sci. Eng. 3 (1995) 689.
[2] H.H.M. Cleveringa, E. Van der Giessen, A. Needleman, Comparison of discrete dislocation and continuum plasticity predictions for a composite material, Acta. Mater. 45 (1997) 3163.
[3] J.P. Hirth, J. Lothe, Theory of Dislocations, first ed., Wiley, New York, 1968.
[4] J. Weertman, J.R. Weertman, Moving dislocations, in: F.R.N. Nabarro (Ed.), Dislocations in Solids, vol. 3, North-Holland, Amsterdam, 1980, p. 1.
[5] J.D. Eshelby, Uniformly moving dislocations, Proc. Roy. Soc. A 62 (1949) 307.
[6] F.C. Frank, On the equation of motion of crystal dislocations, Proc. Roy. Soc. A 62 (1949) 131.
[7] B. Devincre, Meso-scale simulation of the dislocation motion, in: H.O. Kirchner, L.P. Kubin, V. Pontikis (Eds.), Computer Simulation in Materials Science, Nato ASI Series E308, Kluwer, Dordrecht, 1996, p. 309.
[8] P.P. Gillis, J.J. Gilman, J.W. Taylor, Stress dependences of dislocation velocities, Philos. Mag. 20 (1969) 279.
[9] J.P. Hirth, H.M. Zbib, J. Lothe, Forces on high velocity dislocations, Modelling Simul. Mater. Sci. Eng. 6 (1998) 165.
[10] J.Th.M. De Hosson, G. Boom, U. Schlakowski, O. Kanert, Solution hardening in Al–Zn alloys. Mean jump distance and activation length of moving dislocations, Acta Metall. 34 (1986) 1571.
[11] J.Th.M. De Hosson, O. Kanert, A.W. Sleeswijk, Dislocations in solids investigated by means of nuclear magnetic resonance, Chapter in: F.R.N. Nabarro (Ed.), Dislocations in Solids, vol. 6, North-Holland, Amsterdam, 1983, pp. 441–534.
[12] E. Nadgornyi, Dislocation dynamics and mechanical properties of crystals, Prog. Mater. Sci. 31 (1988).
[13] F.R.N. Nabarro, The theory of solution hardening, Philos. Mag. 35 (1977) 613.
[14] F.R.N. Nabarro, in: P.B. Hirsch (Ed.), The Physics of Metals, vol. 2, Cambridge University Press, Cambridge, 1975, p. 164.
[15] U.F. Kocks, A.S. Argon, M.F. Ashby, Thermodynamics and kinetics of slip, Prog. Mater. Sci. 19 (1975).
[16] D. Hull, D.J. Bacon, Introduction to Dislocations, third ed., Pergamon Press, New York, 1984.
[17] U.F. Kocks, The theory of an obstacle-controlled yield strength – report after an international workshop, Mater. Sci. Eng. 27 (1977) 291.